

# Soft X-ray line emission from hot gas in intervening galaxy halos and diffuse gas in the cosmic web

Yuning Zhang<sup>1,\*</sup>, Dandan Xu<sup>1,\*\*</sup>, Chengzhe Li<sup>1</sup>, and Wei Cui<sup>1</sup>

Tsinghua University, Department of Astronomy, 100084, Beijing, China

Received September 30, 20XX

## ABSTRACT

Cosmic hot gas emission is closely related to halo gas acquisition and galactic feedback processes. Their X-ray observations reveal important physical properties and movements of the baryonic cycle of galactic ecosystems. However, the measured emissions toward a target at a cosmological distance would always include contributions from hot gases along the entire line of sight to the target. Observationally, such contaminations are routinely subtracted via different strategies. In this work, we aim at answering an interesting theoretical question regarding the amount of soft X-ray line emissions from intervening hot gases of different origins. We tackle this problem with the aid of the TNG100 simulation. We generated typical wide-field lightcone and estimated their impacts on spectral and flux measurements toward X-ray-emitting galaxy-, group- and cluster-halo targets at lower redshifts. We split the intervening hot gases into three categories, that is, the hot gas that is gravitationally bound to either star-forming or quenched galaxy halos, and the diffuse gas which is more tenuously distributed permeating the cosmic web structures. We find that along a given line of sight, the diffuse gas that permeates the cosmic web structures produces strong oxygen and iron line emissions at different redshifts. The diffuse gas emission in the soft X-ray band can be equal to the emission from hot gases that are gravitationally bound to intervening galaxy halos. While the hot gas emission from the quiescent galaxy halos can be significantly less than that from star-forming halos along the line of sight. The fluxes from all of the line-of-sight emitters as measured in the energy band of 0.4–0.85 keV can reach  $\sim 20\text{--}200\%$  of the emission from the target galaxy, group, and cluster halos. The fluxes from the intervening hot gas as measured in narrow bands around the O VII ( $r$ ) and O VIII ( $K\alpha$ ) are typically only a few percent of the target emission, indicating that these line emissions (as measured within narrow bands) better present the hot gas emission of the target sources, compared to that measured in wider energy bands.

**Key words.** methods: numerical – galaxies: halos – galaxies: intergalactic medium – X-rays: galaxies – techniques: spectroscopic

## 1. Introduction

Hot gas inside gravitationally-bound dark matter halos and extensively permeating the cosmic web structures, is mainly produced by gravitational heating during cosmic structure formation (e.g., Kereš et al. 2005; Dekel & Birnboim 2006; Dekel et al. 2009), or by baryonic feedback processes during galaxy evolution, and typically having a temperature range of  $10^5 \text{ K} \lesssim T \lesssim 10^7 \text{ K}$ . In particular, the heating process is directly linked to various feedback mechanisms of baryonic physics, which eject mass, energy, and momentum to large distances from the galaxy centers, causing galaxy halos suffering from gas depletion at different levels (e.g., Efsthathiou 2000; Cen & Ostriker 2006; Davé & Oppenheimer 2007; Yuan & Narayan 2014; Yuan et al. 2018; Wang et al. 2016; Hopkins et al. 2021; Faucher-Giguère & Oh 2023; Prunier et al. 2025). Theories and simulations have revealed that half of the cosmic baryons are in fact in the form of diffuse hot gas and reside in the large-scale structures. However, this diffuse hot gas component is extremely challenging to observe (Fukugita et al. 1998; Cen & Ostriker 1999; Davé et al. 2001; Kang et al. 2005; Cen & Fang 2006; Bregman 2007; Davé et al. 2010; Shull et al. 2012; Haider et al. 2016; Martizzi et al. 2019).

In the past decades, cosmic and galactic hot gas has become a topic of growing importance to the field of structure forma-

tion and evolution. This is a result of combined advances in both observations and theories through the help of simulations. Current-generation X-ray missions, such as *Chandra*, *XMM-Newton*, *eROSITA* (Predehl et al. 2021), already revealed rich and detailed properties and motions of hot gas in massive galaxies, groups and clusters (Sanders et al. 2020; Zhuravleva et al. 2014, 2019), as well as between galaxy clusters (e.g., gas bridges detected through Sunyaev-Zel’dovich effect in combination with X-ray observations (Planck Collaboration et al. 2013) or direct imaging from X-ray observations (Parekh et al. 2020)). Next-generation X-ray missions, such as the X-Ray Imaging and Spectroscopy Mission (*XRISM*; XRISM Science Team 2020), the Advanced Telescope for High-ENergy Astrophysics (*Athena*; Nandra et al. 2013), the Diffuse Intergalactic Oxygen Surveyor (*Super DIOS*; Yamada et al. 2018), the Hot Universe Baryon Surveyor (*HUBS*; Cui et al. 2020b,a), have been either in place or under planning. Equipped with microcalorimeter-based detector arrays and large mirrors, these next-generation X-ray telescopes with even higher energy resolution (eV-level) and detection efficiencies are dedicated to pushing current detection limits to a further extent.

Our theoretical understanding about hot gas physics has also been making steady progress, in particular since the advent of state-of-the-art cosmological hydrodynamical simulations (e.g., Crain et al. 2010; van de Voort & Schaye 2013; Nelson et al. 2018a; Oppenheimer et al. 2020b,a; Wijers & Schaye 2022; Nelson et al. 2023), including those recent dedicated cluster sim-

\* E-mail: zhangyuning@mail.tsinghua.edu.cn

\*\* E-mail: dandanxu@tsinghua.edu.cn

ulation suites within a cosmological context (TNG-Cluster simulation, see Nelson et al. 2024; Lehle et al. 2024; Truong et al. 2024; Rohr et al. 2024; Ayromlou et al. 2024).

For example, Oppenheimer et al. (2020a) made specific mock observations for the *eROSITA* instrument on the Spectrum-Roentgen-Gamma mission (Merloni et al. 2012) using the IllustrisTNG (Pillepich et al. 2018a; Marinacci et al. 2018; Nelson et al. 2018b; Springel et al. 2018; Naiman et al. 2018) and the EAGLE (Schaye et al. 2015) simulations. They found that the hot circumgalactic medium (CGM) emission in central galaxies with lower masses and higher specific star formation rate (sSFR) can be detected out to a distance of 30–50 kpc, while in higher-mass central galaxies this detection can go out to 150–200 kpc. Both simulations also predicted higher soft X-ray luminosities (at fixed stellar mass) for higher-sSFR galaxies, in comparison to their lower-sSFR galaxy counterparts. Using three suits of hydrodynamical simulations, that is, EAGLE, IllustrisTNG, and SIMBA (Davé et al. 2019), Schellenberger et al. (2024) demonstrated the feasibility of characterizing the CGM in nearby galaxy halos ( $z \sim 0.01$ – $0.03$ ) using next-generation X-ray microcalorimeter. Through the mock spectroscopic observations made with typical instrumental design parameters, they found that individual halos of Milky Way mass can be traced out to large distances using prominent emission lines, such as O VII, O VIII and iron lines. They also demonstrate the ability of X-ray observations to reveal the spatial distributions of temperature, velocity, and abundance ratio through spectral fitting for individual galaxy halos.

One shall note that observationally accurate and clean measurement of any given target X-ray source at a cosmological distance is not an easy task, simply because the total detected emission also includes contamination from the Milky Way foreground (e.g., Ponti et al. 2023; Locatelli et al. 2024) as well as from all emitters along the entire line of sight. In light of next-generation X-ray missions equipped with microcalorimeters, our previous study (Zhang et al. 2022) showed that with a spectral resolution as high as 2 eV, the bright X-ray emission lines (such as O VII and O VIII) from targets at redshifts beyond  $z \sim 0.01$  will be able to be separated from the Milky Way foreground emissions. This is also highlighted by Schellenberger et al. (2024), which showed the necessity of implementing microcalorimeters at a spectral resolution as high as 2 eV to distinguish the faint CGM line emission from the target sources from the bright Milky Way foreground emission.

Regarding the line-of-sight contamination, Chadayammuri et al. (2022) detected spatially resolved CGM in both star-forming and quiescent galaxies by stacking the X-ray observations of optically selected galaxies between  $0.01 < z < 0.1$  in the *eROSITA* Final Equatorial Depth Survey (eFEDS), and the results were compared to the IllustrisTNG and Eagle cosmological simulations. In order to subtract contribution from the hot halo emission originated in groups and clusters that lie along the line of sight either in the foreground or background to the targeted galaxies, they removed these extended sources by cross-matching the eFEDS group and cluster catalog (Liu et al. 2022), which contains 542 candidate groups and clusters in the redshift range of 0.01 to 1.3, with a median redshift of 0.35. It turned out that only 37 of 2643 targeted galaxies lie within a projected distance of twice  $R_{500}$  from a group or cluster. To further remove X-ray emission from diffuse hot gas along the line of sight, they subtracted from the stacked signal the median of the average emission within an annulus of 150–300 kpc from each galaxy in the stacked sample, assuming that the target emission will not go beyond 100 kpc. Using a

similar approach through stacking the X-ray emission from galaxies in the *SRG/eROSITA* All-Sky Surveys, Zhang et al. (2024) detected hot CGM in Milky Way-mass and M31-mass galaxy halos out to  $z = 0.2$  and found that the baryon budget in the hot halo gas is lower than the  $\Lambda$ CDM prediction, indicating significant gas depletion in halos at these scales. In their study, contamination effects from satellite galaxies were dealt with by carefully constructing galaxy samples using spectroscopic redshifts and comparing to cosmology simulations.

The primary goal of this study is, using cosmological simulations and through identifying and characterizing the hot gas across a range of redshift, to theoretically explore the significance of soft X-ray emission from different intervening components along some typical line of sight in light of high-energy resolution soft X-ray spectroscopic observations. In particular, we compare among the line-of-sight emissions from the diffuse gas components, star-forming galaxy halos, and quiescent galaxy halos, and we also compare the total emissions from the entire line-of-sight emitters to the emission from the target galaxy, group, and cluster halos. We find that the diffuse gas produces strong oxygen and iron line emissions at different redshifts, contributing almost equally to hot gas gravitationally bound to intervening galaxy halos; while star-forming galaxy halos contribute more line emissions than quiescent galaxy halos along the line of sight. In general, line emissions as measured in narrow bands around the O VII ( $r$ ) and O VIII ( $K\alpha$ ) can better present the hot gas emission of the target sources, as the contributions from the line of sight emitters are typically a few percent of the target emission; while the line-of-sight emission measured in a broader soft X-ray energy bands can reach several tens percent of the target emission.

The remaining part of this paper proceeds as follows. In Sect. 2, we present the simulation data, the method of producing the lightcone, the classification of the gas and how to calculate the X-ray emission. The results on the gas in the lightcone are shown in Sect. 3. Finally, we give the discussion and the conclusions of this work in Sect. 4.

## 2. Methods

### 2.1. Numerical simulation

In this work, we use data from the IllustrisTNG project<sup>1</sup> (TNG hereafter; Pillepich et al. 2018a; Marinacci et al. 2018; Nelson et al. 2018b; Springel et al. 2018; Naiman et al. 2018), which is one of the state-of-the-art large cosmological magnetohydrodynamical simulations. The main scientific goal of the TNG project is to shed light on the key physical processes of cosmic structure formation and evolution. The TNG simulation was performed with a parallel moving-mesh code AREPO (Springel 2010). The galaxy formation model of TNG includes gas radiative cooling, star formation, stellar evolution, chemical enrichment, black hole formation, growth, and multimode feedback (Weinberger et al. 2017; Pillepich et al. 2018b). The TNG simulation suite includes three primary runs: TNG50, TNG100, and TNG300. Each run has been carried out at three resolution levels. In this work, we adopt the full baryonic physics data of TNG100-1, which have moderate size (the box side length is  $L_{\text{box}} = 110.7 \text{ Mpc}$ ) and high resolution (the dark matter and mean baryon particle mass resolutions are  $m_{\text{DM}} = 7.5 \times 10^6 M_{\odot}$  and  $m_{\text{baryon}} = 1.4 \times 10^6 M_{\odot}$ , respectively). Dark matter halos and galaxies hosted within are identified using the Friends-of-Friends (FoF) (Davis et al. 1985) and SUBFIND (Springel et al.

<sup>1</sup> <http://www.tng-project.org/>

2001; Dolag et al. 2009) algorithms, respectively. The simulation and this work adopt the standard  $\Lambda$ CDM cosmological parameters advanced by Planck Collaboration et al. (2016), namely dark energy density parameter  $\Omega_\Lambda = 0.6911$ , matter density parameter  $\Omega_m = 0.3089$ , baryon density parameter  $\Omega_b = 0.0486$ , power spectrum normalization characterized by  $\sigma_8 = 0.8159$ , scalar spectral index  $n_s = 0.9667$  and dimensionless Hubble constant  $h = 0.6774$ .

The TNG data release include the snapshots and halo (subhalo) catalogs at each snapshot (Nelson et al. 2019). The halo (subhalo) catalogs include FoF and SUBFIND objects. The snapshot data include all simulation particles and cells. We note that any given FoF halo may contain one or more subhalos. The particles/cells belonging to subhalos are gravitationally bound. While the diffuse and gravitationally unbound particles/cells are in general referred to as “fuzz” elements. Depending on whether they belong to any FoF halo, the “fuzz” particles/cells can be further divided into the “inner fuzz” or the “outer fuzz.” The gas cells belonging to these different categories are used to construct our light cones. We note that this “fuzz” component physically includes all hot gas that is not gravitationally bound to any galaxies and dark matter halos, including intracluster medium (ICM), intragroup medium (IGrM), and intergalactic medium (IGM) permeating the cosmic web. ICM is the diffuse hot gas that resides in a cluster of galaxies but does not belong to any substructures of the cluster (Ryden & Pogge 2021). IGrM is similar to ICM but for group of galaxies. In simulation, these types of gas can be classified as “inner fuzz” cells that belong to a FoF-group but are not bound to any SUBFIND subhalo. On the contrary, the IGM can be well approximated by the “outer fuzz” in simulation, since this diffuse gas component does not belong to any groups/halos.

## 2.2. Simulated wide-field lightcone

In order to study the contribution of X-ray emission from hot gas along any given line of sight but outside a target source, we constructed a simulated lightcone. We can link the discrete redshift outputs of the numerical simulation with practical observations. In particular, to study the properties of the hot gas in the filamentary structures, a wide-field lightcone is needed.

In this work, we adopt the method of Kitzbichler & White (2007) to construct a simulated lightcone without repeated structures. Once a pair of integers  $(n, m)$  without common factor has been chosen, the corresponding line of sight, field of view, and observation redshift range are uniquely determined. More detailed description of this method can be found in Kitzbichler & White (2007, Sect. 2.4.1).

Considering the box size of TNG100, we choose a pair of integers  $(n, m) = (4, 3)$  to obtain the simulated wide-field lightcone with FoV of  $\sim 1.59^\circ \times 1.19^\circ$  and redshift range of  $z = 0-0.356$ . We note that this redshift range is far beyond the target galaxy, group, and cluster halos at cosmological distances that are expected and plausible to observe using next-generation X-ray telescopes for case study (Zhang et al. 2022). In this work, we use the central square area with the field of  $1^\circ \times 1^\circ$  as the angular coverage of the lightcone.

## 2.3. Component identification

Hot gas within any given line of sight but outside the target source has two major origins, that is, gravitationally bound galaxies and their dark matter halos, and diffuse gas in the intergalactic medium between galaxy halos. Apart from evaluating

their X-ray emission in the lightcone and making comparisons to emission from the target source, it is also interesting to compare the X-ray emission from hot gas of different origins. For this reason, we categorized the gas cells in the lightcone into several types corresponding to different observational characteristics.

First, we consider the hot gas gravitationally bound to the galaxy halos. To guarantee that the galaxies have enough baryonic mass to be sufficiently resolved, we only select the subhalos with stellar mass of  $M_* > 5 \times 10^9 M_\odot$ , where  $M_*$  is the sum of masses of all stars within twice the stellar half mass radius. We note that only 5.33 % of the total gas mass resides in subhalos below this stellar-mass threshold. According to their star formation activities, we further split the selected galaxies into a subsample of star-forming galaxies and a subsample of quenched galaxies. The method we use to identify different types of galaxies is similar to the practice of Genel et al. (2018) and Lu et al. (2021), which we roughly summarize below. We calculate the mean specific star formation rate ( $\text{sSFR} = \text{SFR}/M_*$ ) within twice the stellar half mass radius of these subhalos in a snapshot. The sSFR of subhalo as a function of the stellar mass at  $z = 0.01$  is shown in Fig. 1. Galaxies that lie below 1 dex below the mean sSFR are classified as quenched galaxies. We refer to galaxies above this threshold as star-forming galaxies. Such a classification was consistently carried out at different redshifts for this study. In addition, we have also identified a diffuse gas component in the lightcone as the collection of all “fuzz” gas cells, that is, including the ICM and IGrM (classified as “inner fuzz”), as well as IGM (“outer fuzz” in simulation).

Table 1 lists the total numbers of star-forming and quenched galaxies, and the total amount of stellar mass and gas mass, contained in the investigated lightcone (LC0) of  $1^\circ \times 1^\circ$  field of view. It can be seen that the number of star-forming galaxies is significantly greater than that of quenched galaxies. However, the total stellar mass and total gas mass are similar among the two types of galaxies, as the latter samples are more massive than the former in general. In comparison, the diffuse gas component takes up the highest mass fraction in comparison to gas bound to galaxies, about five times the latter. This finding is broadly consistent with the study of Galárraga-Espinosa et al. (2021), which found that the warm-hot intergalactic medium in filament accounts for  $\sim 80\%$  of the local baryon budget using the TNG300 simulation. Such a component being the major part of the diffuse gas, is also the primary candidate for the “missing baryons” in the local universe (e.g., Cen & Ostriker 1999; Phillips et al. 2001; Yoshikawa et al. 2003; Nicastro et al. 2005, 2008; Kaastra et al. 2013; Nicastro et al. 2018).

We note that, given the investigated field of view, the hot gas emission can markedly differ among different lines of sight. In principle, one shall generate a sample of lightcones for such analyses in order to better assess the scatter. However, as the calculation of the hot gas emission is already extensive for one lightcone, we have also generated another eight different lightcones only to examine the numbers of intervening galaxies, and the amount of baryonic masses in these lightcones for comparisons. We have not carried out any further calculations for the hot gas emission therein. The statistical results are also listed in Table 1. As can be seen, LC0 is a line of sight that is on the lower side in terms of the number of intervening galaxies and the amount of mass in baryons. In the next sections, we present the results of the hot gas emission in the case of LC0.

Table 1: A summary on star-forming and quenched galaxies and diffuse gas per square degree in the simulated lightcones (constructed up to  $z = 0.356$ ).

	Type	Number of galaxies	Total stellar mass ( $M_{\odot}$ )	Total gas mass ( $M_{\odot}$ )
LC0	Star-forming galaxies	1174	$3.299 \times 10^{13}$	$1.114 \times 10^{14}$
	Quenched galaxies	459	$3.847 \times 10^{13}$	$1.332 \times 10^{14}$
	Diffuse gas	–	–	$1.324 \times 10^{15}$
LC1	Star-forming galaxies	1217	$3.426 \times 10^{13}$	$1.283 \times 10^{14}$
	Quenched galaxies	669	$5.376 \times 10^{13}$	$2.290 \times 10^{14}$
	Diffuse gas	–	–	$1.418 \times 10^{15}$
LC2	Star-forming galaxies	1306	$3.830 \times 10^{13}$	$1.450 \times 10^{14}$
	Quenched galaxies	675	$5.395 \times 10^{13}$	$2.448 \times 10^{14}$
	Diffuse gas	–	–	$1.410 \times 10^{15}$
LC3	Star-forming galaxies	1683	$5.236 \times 10^{13}$	$2.004 \times 10^{14}$
	Quenched galaxies	868	$6.501 \times 10^{13}$	$2.369 \times 10^{14}$
	Diffuse gas	–	–	$1.711 \times 10^{15}$
LC4	Star-forming galaxies	1272	$3.852 \times 10^{13}$	$1.641 \times 10^{14}$
	Quenched galaxies	577	$4.175 \times 10^{13}$	$1.317 \times 10^{14}$
	Diffuse gas	–	–	$1.421 \times 10^{15}$
LC5	Star-forming galaxies	1222	$3.539 \times 10^{13}$	$1.418 \times 10^{14}$
	Quenched galaxies	518	$4.242 \times 10^{13}$	$1.559 \times 10^{14}$
	Diffuse gas	–	–	$1.343 \times 10^{15}$
LC6	Star-forming galaxies	1300	$3.412 \times 10^{13}$	$1.241 \times 10^{14}$
	Quenched galaxies	554	$4.419 \times 10^{13}$	$1.599 \times 10^{14}$
	Diffuse gas	–	–	$1.411 \times 10^{15}$
LC7	Star-forming galaxies	1389	$4.320 \times 10^{13}$	$1.684 \times 10^{14}$
	Quenched galaxies	666	$5.162 \times 10^{13}$	$1.852 \times 10^{14}$
	Diffuse gas	–	–	$1.481 \times 10^{15}$
LC8	Star-forming galaxies	1427	$4.227 \times 10^{13}$	$1.657 \times 10^{14}$
	Quenched galaxies	665	$5.142 \times 10^{13}$	$1.598 \times 10^{14}$
	Diffuse gas	–	–	$1.490 \times 10^{15}$

Note: for the “Diffuse gas” in the third line in each lightcone row, the last column “Total gas mass” is calculated as the sum of masses of all the “fuzz” gas particles in the lightcone. Whereas for either “Star-forming galaxies” or “Quenched galaxies” in the first or second line in each lightcone row, the “Total gas mass” and the “Total stellar mass”, respectively, are calculated as sums of all gas masses and stellar masses of subhalos located in a given lightcone. Counting particles (belonging to subhalos) instead will yield slightly smaller values due to boundary cut-off of the lightcone.

#### 2.4. X-ray emission calculation

The hot, X-ray-emitting gas is usually assumed to be optically thin and in collisional ionization equilibrium (CIE). To model this gas, we adopt the Astrophysical Plasma Emission Code (APEC v3.0.9; Smith et al. 2001; Foster et al. 2012). Using the Simulated Observations of X-ray Source (SOXS; ZuHone et al. 2023) package, we calculate the X-ray emission of the gas with the APEC model. For each gas cell, to derive its X-ray emission, we input its local density, temperature, and metallicity into the code. It should be noted that the metallicity value should be converted to solar metallicity by dividing by 0.0127 (the primordial solar metallicity used in TNG; Wiersma et al. 2009). Furthermore, the X-ray emission should be Doppler-shifted and cosmologically redshifted according to the peculiar velocity and the redshift of the gas cell. In practice, the soft X-ray energy band on which we focused is 0.1–2 keV. This band includes many interesting metal lines, such as, O VII triplets (0.561 keV, 0.569 keV and 0.574 keV), O VIII  $K\alpha$  line (0.654 keV) and a series of Fe XVII lines (e.g., 0.725 keV, 0.727 keV, 0.739 keV and 0.826 keV).

### 3. Results

The hot gas in dark matter halos is multiphase (Putman et al. 2012; Tumlinson et al. 2017; Péroux & Howk 2020). In our previous study (Zhang et al. 2022), we used the TNG100 simulation to investigate the soft X-ray emission properties of hot gases in galaxy-, group- and cluster-sized dark matter halos. We demonstrated that the hot gas of different phases and with different origins broadly spreads out in its observational characteristics. In that study, we made exact mock observations of the hot CGM emission therein for the *HUBS* mission<sup>2</sup> (Cui et al. 2020b,a). This process included generating X-ray spectra from these targets using the APEC code and sampling the spectra to make mock observations using PyXSIM, accounting point-like emissions from unresolved AGN population as the main component of the cosmic X-ray background, as well as adding the Milky Way foreground emission using the SOXS package. In this study, we do not aim at making any exact mock observations with all realistic components for any specific X-ray missions, but evaluate from a theoretical perspective the amount of soft X-ray emission from hot gases in hundreds and thousands of galaxies as

<sup>2</sup> <https://hubs-mission.cn/en/index.html>

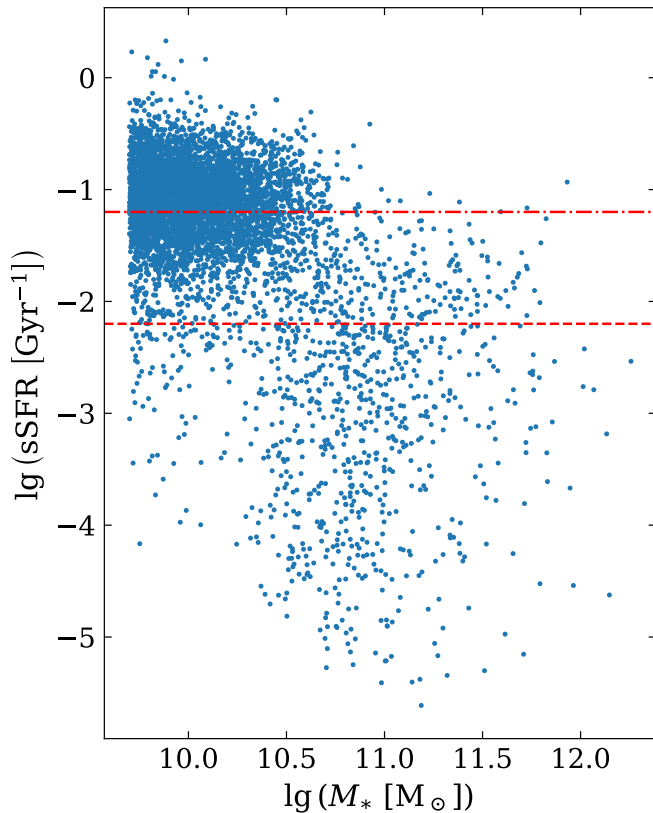


Fig. 1: The specific star formation rate (sSFR) as a function of stellar mass for all galaxies at  $z = 0.01$  (snapshot 98). The stellar mass here is calculated using all stellar particles within twice the stellar half mass radius of a given subhalo. The red dash-dotted line represents the mean sSFR. The red dashed line represents 1 dex below the mean sSFR, below which galaxies are classified as quenched galaxy populations (e.g., Lu et al. 2021).

well as from the warm-hot intergalactic medium that permeates the cosmic web along typical lines of sight toward interesting targets.

### 3.1. Emissivity maps

In order to evaluate the contribution of line-of-sight emissions and make comparisons to the target source emission, in this work, we use three types of X-ray targets that were previously studied in Zhang et al. (2022). The three targets are a galaxy halo with a total mass of  $M = 3.06 \times 10^{12} M_{\odot}$  at  $z = 0.03$ , a group halo of  $M = 7.00 \times 10^{13} M_{\odot}$  at  $z = 0.11$ , and a cluster halo of  $M = 3.78 \times 10^{14} M_{\odot}$  at  $z = 0.11$ . As shown in Zhang et al. (2022), these targets are ideal for soft X-ray emission imaging and spectroscopic studies. In Fig. 2, we present the X-ray emissivity maps of the selected targets. We use them as references to evaluate and compare emissions from lightcone intervening galaxies and diffuse gas along the lines of sight to these targets. In the figure, we label the  $R_{200c}$  (within which the mean density is equal to 200 times the cosmological critical density) of the target sources with white dash-dotted circles.

We refer to the emission of all intervening galaxies and diffuse gas in the lightcone as the lightcone emission, which is calculated using the lightcone (LC0) that we have constructed up to  $z = 0.35$  from the simulation (see Sect. 2 for detailed discus-

sion). In order to study the average behavior and the variance of the lightcone emission, we selected five subregions, labeled R0, R1, R2, R3 and R4 in each case. Each subregion is set to have a radius of  $R_{200c}$  of the target source. The soft X-ray emissivity maps of the lightcone are shown in Fig. 3, where the three panels present the corresponding subregion locations in each of the target cases.

### 3.2. Hot gas phase-space properties

Previous studies of the phase-space properties of hot gas in the simulation are limited to single snapshot at the target source redshift (Torrey et al. 2019; Martizzi et al. 2019; Artale et al. 2022). In this work, we take an entire lightcone into account, and present in Fig. 4 the phase-space diagrams of the hot gas in different components of the lightcone. These phase-space diagrams present 2D histograms of the mass fraction of gas with respect to the total gas mass in the density-temperature plane and in the metallicity-temperature plane, respectively. We make separate plots for the phase diagrams of gas residing in star-forming galaxies, quenched galaxies, and diffuse gas, respectively.

As Fig. 4 shows, there are apparent differences between the phase diagrams of different kinds of gas. The long and narrow stripe feature in the diagram comes from star-forming gas, which is put on the effective equation of state by the multiphase star-formation subgrid model (Springel & Hernquist 2003). Star-forming galaxies contain more star-forming gas than the quenched galaxies, while the diffuse gas component contains least star-forming gas, but extends to much lower density regions. The temperatures of gas that is strongly gravitationally bound to galaxies are close to  $\gtrsim 10^4$  K with a clear density floor of  $\sim 10^{-29} \text{ g cm}^{-3}$  (Vogelsberger et al. 2012). The majority of gas in star-forming galaxies is in the temperature range of  $\sim 10^5$ – $10^{7.5}$  K and in quenched galaxies,  $\sim 10^6$ – $10^{7.5}$  K. As galaxies are condense gas and metal reservoirs and severely suffer from chemical enrichment, the majority of gas in galaxies is located within a metallicity range of  $\sim 0.1$ – $1 Z_{\odot}$ . While the diffuse gas exhibits much lower metallicities.

### 3.3. Spectra

We extract signals from the selected regions to make the emission spectra. The example spectra (within the energy band that contains abundant strong emission lines) of the selected regions in the lightcone are shown in Figs. 5, 6, and 7. For comparison, the spectra of the targets were also plotted in these figures. In each case, we present two extreme situations in which the target is the most and least significantly contaminated by intervening emissions from the lightcone.

As can be seen, the spectra from the lightcone contain abundant emission lines at different redshifts. In particular, strong emission lines in this given energy band include Fe xvii lines, O vii, and O viii lines. Observationally, when several (identified) emission lines correspond to the same redshift, they can be taken as coming from a common origin. In most cases, bright emission lines from the targets are much stronger than those from the intervening structures. In particular, in the case of galaxy clusters, because of the high temperature of the hot gas therein, continuum emission significantly dominates the spectra. However, there are cases where the X-ray emission from the intervening components along the line of sight becomes significantly strong (e.g., the top panels in Fig. 6 and Fig. 7). We note that the soft X-ray spectra of star-forming galaxies contain more abundant emis-



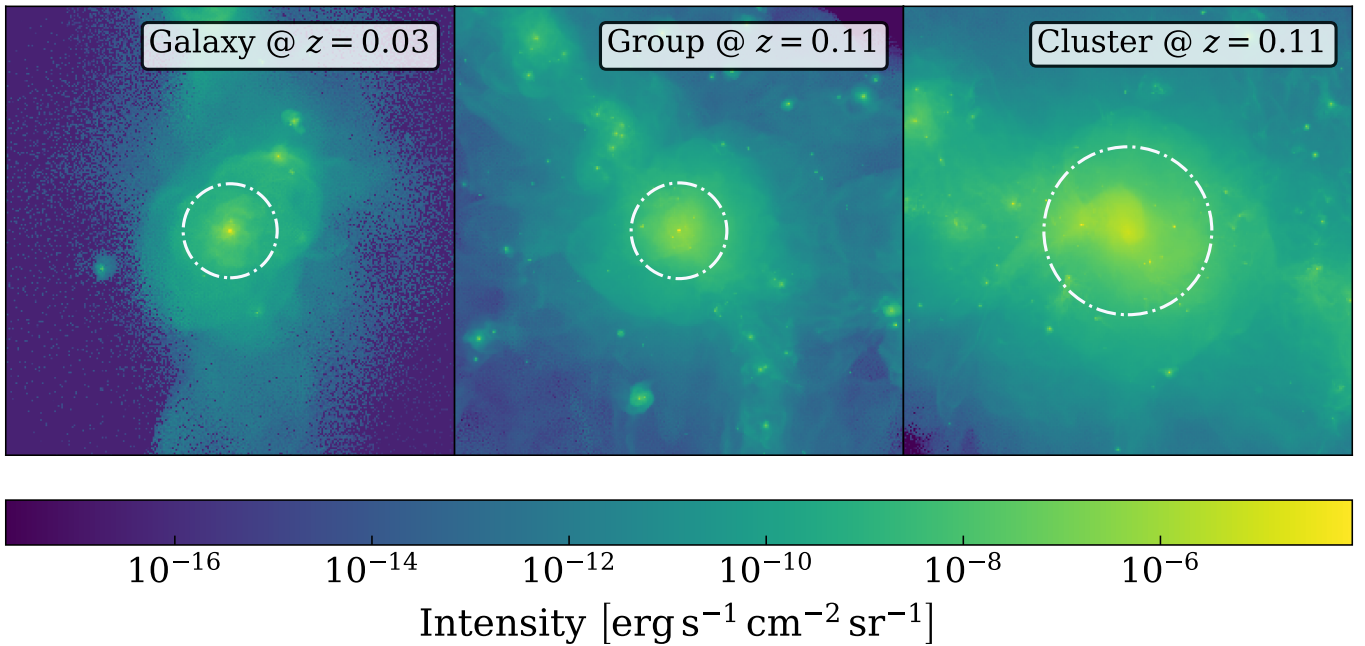


Fig. 2: X-ray emissivity maps of the observation targets only, i.e., generated using all gas particles bound to the target halos, no emissions from the foreground or background added to the map. The X-ray energy range is 0.1–2 keV. Panels from left to right: a galaxy with a total mass of  $M = 3.06 \times 10^{12} M_{\odot}$  at  $z = 0.03$ , a galaxy group with a total mass of  $M = 7.00 \times 10^{13} M_{\odot}$  at  $z = 0.11$ , and a galaxy cluster with a total mass of  $M = 3.78 \times 10^{14} M_{\odot}$  at  $z = 0.11$ . Each panel is  $256 \times 256$  in dimension, corresponding to a sky region of  $1^{\circ} \times 1^{\circ}$ . The white dash-dot circle denotes  $R_{200c}$  of the target.

sion lines than quenched galaxies (regarding this, we present a detailed quantitative comparison in Table 2 from Sect. 3.4). While the spectra of diffuse gas contain the most abundant strong metal lines, especially Fe xvii lines. In addition, low-mass systems galaxies tend to contribute more to the strong O vii lines, while high-mass systems (e.g., massive groups and clusters) tend to generate stronger continuum and more abundant iron lines. We note that properly resolving emission lines is critical in distinguishing hot gas emissions from the targets and from the intervening components along the lines of sight.

### 3.4. Fluxes within observed energy bands

Table 2 summarizes the X-ray flux ratios between the lightcone emission (in the selected subregions) and the targets (both within  $R_{200c}$  of the target) within four different observed energy bands, including a full soft X-ray band in 0.1–2 keV, a narrower band in 0.4–0.85 keV (as presented in Figs. 5, 6 and 7), and two narrow bands one around the strongest line (a resonance line with a centroid rest-frame energy of 0.574 keV) in the O vii triplet and one around O viii of the target sources. For the emission lines, the line centroid was identified by SPECUTILS (Earl et al. 2022) and the flux was calculated using a line-width of 4 eV. As can be seen, despite the situation varying case by case, the overall lightcone emission in 0.1–2 keV (as presented in the very last row in the table) can reach 10–30 % of the target flux level, already indicating a nonnegligible contribution from the line-of-sight hot gas to the total emission. While the situation is more severe for the energy band of 0.4–0.85 keV (as presented in the second-to-last row in the table). In the three cases that were used as the target sources in this study, the lightcone emission (as from intervening emitters alone) within this energy range can reach 30–80 %, 30–200 % and 20–40 % the fluxes of the target

galaxy, group, and cluster, respectively. In particular, the lightcone emission takes the lowest fraction in the case of cluster, this is simply because the target cluster has much stronger X-ray emission within this energy range. For narrow-band fluxes measured around the O vii and O viii lines of the target sources (presented in the third- and fourth-to-last rows of the table), the lightcone contamination can reach  $\sim 20\%$  in a few cases. However, in most cases, the fluxes in these oxygen lines from the targets are significantly higher than the intervening emission by at least one order of magnitude, suggesting that these oxygen line emissions (as measured within narrow bands) are better tracers of the hot gas emission from the target sources, in comparison to that measured in wider energy bands.

We further make a distinction between the hot-gas emissions from star-forming galaxy halos, quenched galaxy halos, and diffuse gas in the lightcone. We first present Fig. 8, which shows the X-ray fluxes of all line-of-sight galaxies versus intervening diffuse gas both projected within the selected subregions. From this figure we can see that fluxes within the full band between 0.1–2 keV from intervening galaxies are generally stronger than fluxes of diffuse gas in most cases. Whereas the fluxes within the energy band between 0.4 keV to 0.85 keV (as given under shaded areas), which contains strong Oxygen and Iron lines, are similar between the galaxy emission and diffuse gas emission. Figure 9 presents a comparison between line-of-sight star-forming and quenched galaxies within the subregions. As can be seen, star-forming galaxies contribute significantly more emissions than quenched galaxies in all cases. We note that cosmological simulations typically predict that star-forming galaxies are X-ray brighter than quiescent galaxies (at fixed stellar mass) (see Truong et al. 2020; Robson & Davé 2020; Oppenheimer et al. 2020a), as the former produces a significant amount of X-ray emission into the hot halo due to

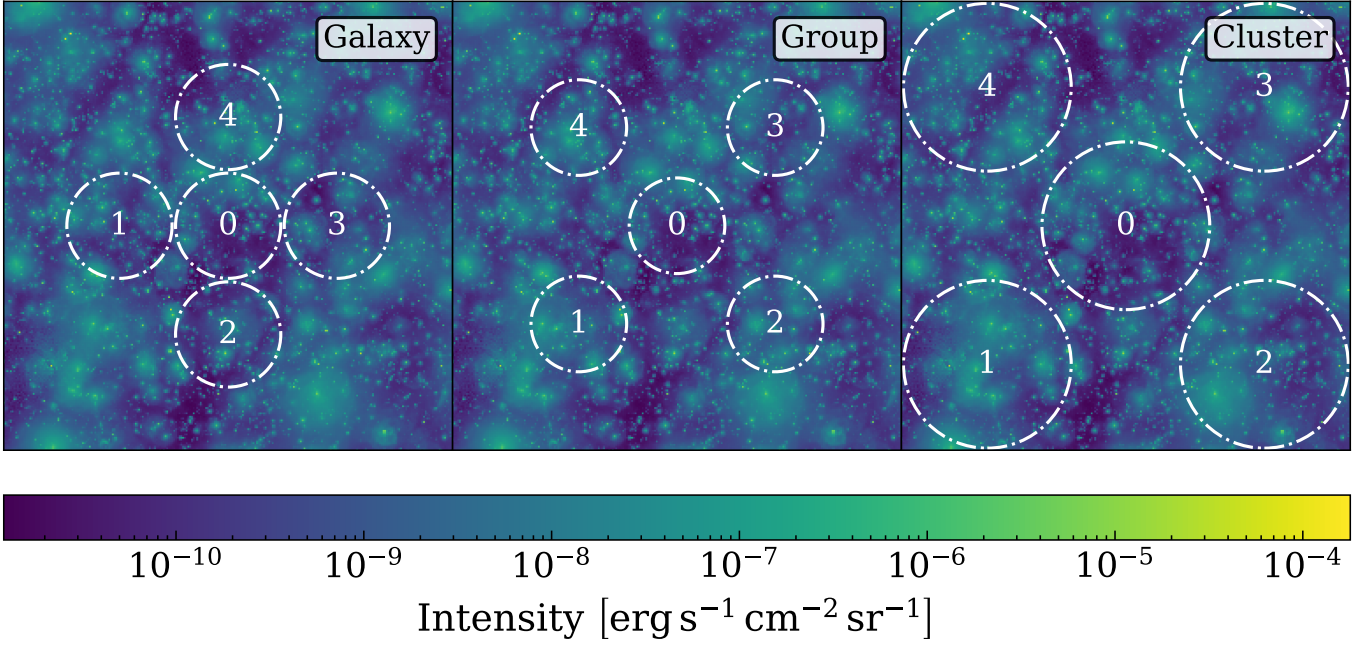


Fig. 3: X-ray emissivity maps of the lightcone with FoV of  $1^\circ \times 1^\circ$ . In each of the three panels from left to right, we select five subregions (indicated by white dash-dotted circles) that have radii of  $R_{200c}$  corresponding to the target galaxy, group, and cluster (as given in Fig. 2), respectively.

stellar feedback (e.g., Sarkar et al. 2016; Fielding et al. 2020), while the latter are typically quenched via high-speed outflow pushing hot gas out of the dark matter halo by the central supermassive black hole feedback. These simulation results are broadly consistent with high-resolution X-ray observations from the *Chandra* and *XMM-Newton*, which detected luminous X-ray coronae around massive spiral galaxies and hotter halo gas around lower-mass galaxies likely due to stellar feedback (e.g., Anderson & Bregman 2011; Bogdán et al. 2015, 2017; Li et al. 2017, 2018; Das et al. 2019). Stacked *eROSITA* observations also revealed that CGM around more massive or star-forming galaxies exhibit higher X-ray luminosities out to 100 kpc than their lower-mass or quiescent counterparts (Chadayammuri et al. 2022).

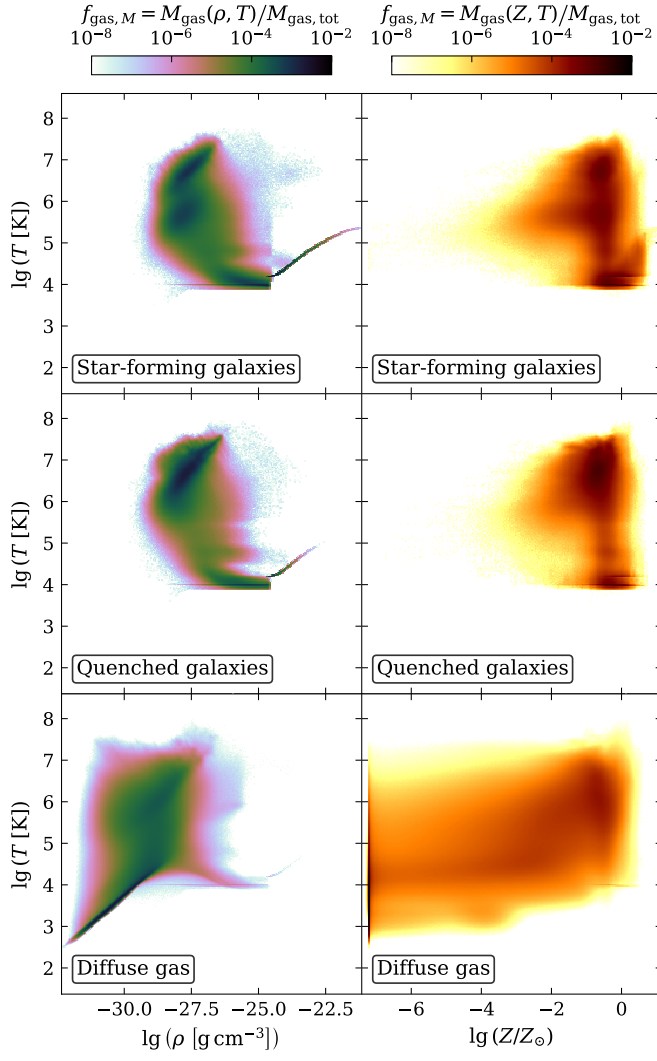


Fig. 4: The phase-space diagrams of gas in the lightcone. The left-hand side panels: temperature versus density. The right-hand side panels: temperature versus metallicity. Panels from top to bottom: star-forming galaxies, quenched galaxies, and diffuse gas. The color maps represent the mass fraction of gas with respect to the total gas mass.



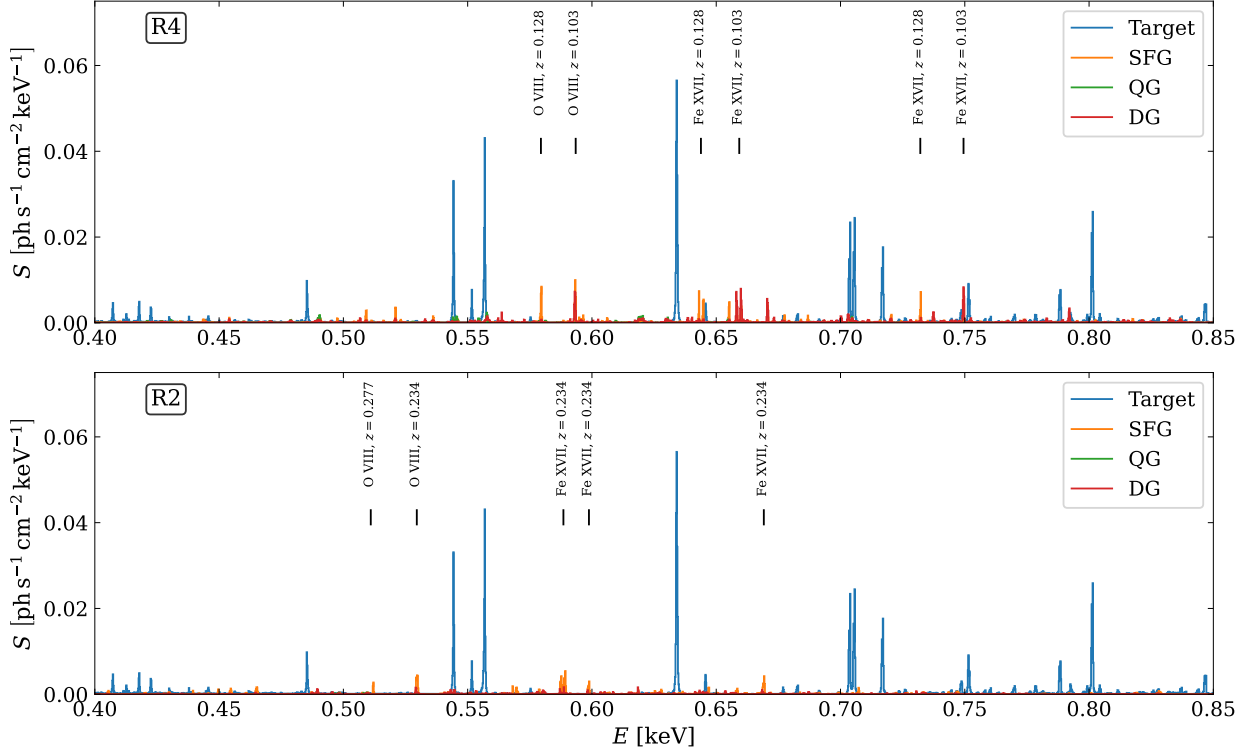


Fig. 5: Two example combined spectra of the target galaxy (blue) and lightcone emission in two selected subregions (R2 and R4). The spectrum energy range shown here is 0.4–0.85 keV and the bin width is 0.2 eV, calculated within a radius of  $R_{200c}$  of the target galaxy, centered on the galaxy. The top panel presents spectra of a subregion (R4) with abundant strong emission lines from the lightcone. The bottom panel shows spectra of a subregion (R2) with less abundant emission lines from the lightcone. The labeled vertical black bars denote the most significant emission lines in the lightcone, with identities and redshifts tagged. SFG represents star-forming galaxies, QG represents quenched galaxies, DG represents diffuse gas.

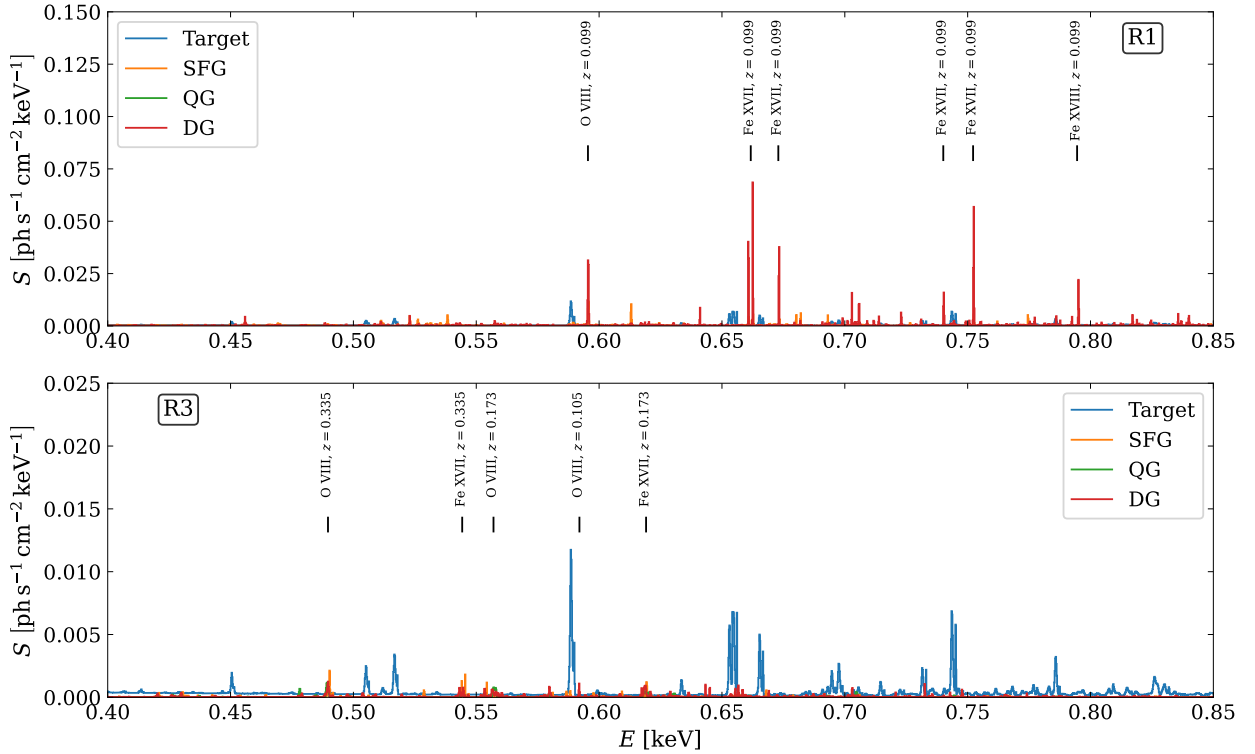


Fig. 6: The same as Fig. 5, but for the target group. we note that the emission from the target group (blue) is the same in both panels. Subregion R1 has much more significant lightcone emission than subregion R3.

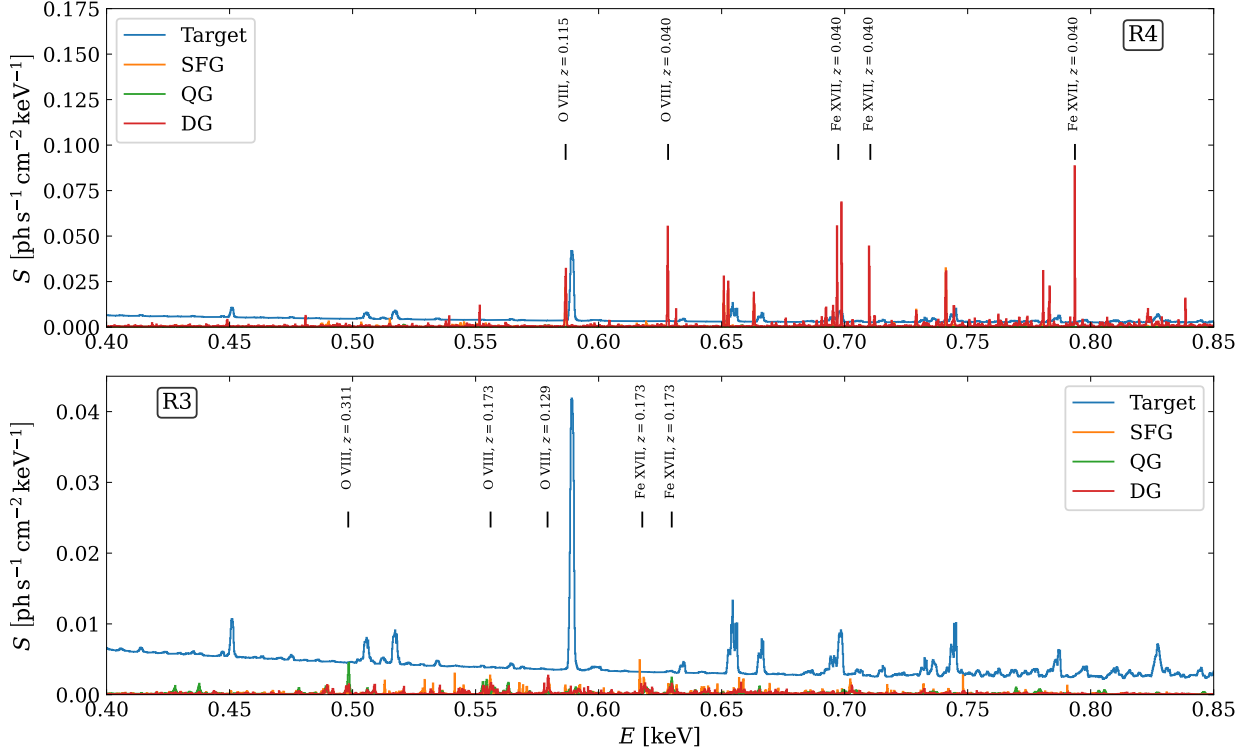


Fig. 7: The same as Fig. 5, but for the cluster. We note that the emission from the target cluster (blue) is the same in both panels. Subregion R4 has much more significant lightcone emission than subregion R3.

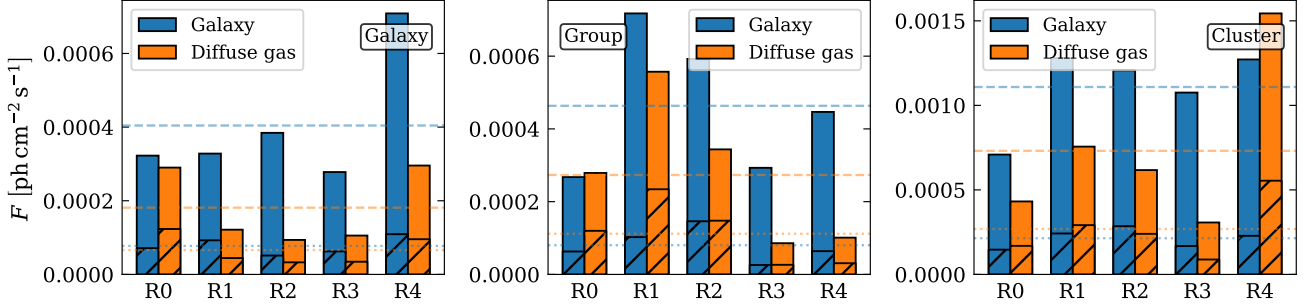


Fig. 8: X-ray fluxes from line-of-sight galaxies (blue) and diffuse gas (orange) in different subregions. Panels from left to right correspond to the three cases, targeting at a galaxy, a group, and a cluster (as given in Fig. 2), respectively. The shadow areas represent the fluxes between 0.4 keV and 0.85 keV. The dash lines represent the mean values of the fluxes among five subregions in each case. The dotted lines represent the mean values in the shadow parts.

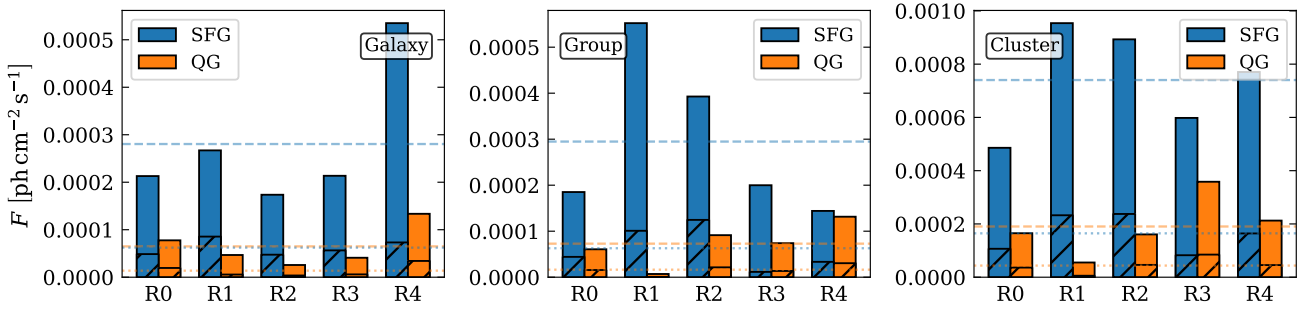


Fig. 9: The same as Fig. 8, but for a comparison between line-of-sight star-forming galaxies (blue) and quenched galaxies (orange).

Table 2: The X-ray flux ratios between the selected regions in the lightcone and the targets.

Type		Galaxy						Group						Cluster					
		R0	R1	R2	R3	R4	mean	R0	R1	R2	R3	R4	mean	R0	R1	R2	R3	R4	mean
		flux ratio between the lightcone and the target (%)						flux ratio between the lightcone and the target (%)						flux ratio between the lightcone and the target (%)					
Star-forming galaxies	O VII (r)	0.72	1.07	0.41	1.27	4.83	1.66	3.13	10.53	4.21	0.23	11.67	5.95	1.29	2.40	2.14	2.15	7.23	3.04
	O VIII (K $\alpha$ )	0.64	1.18	0.91	1.46	1.47	1.13	2.61	14.33	7.64	2.29	5.12	6.40	0.97	9.87	3.57	1.28	1.39	3.42
	0.4–0.85 keV	20.25	35.59	19.73	23.50	30.47	25.91	24.45	55.80	68.89	6.40	18.47	34.80	5.71	12.43	12.69	4.41	8.78	8.81
	0.1–2 keV	7.15	8.97	5.83	7.17	17.97	9.42	3.88	11.56	8.22	4.19	3.02	6.17	4.12	8.09	7.57	5.07	6.53	6.28
Quenched galaxies	O VII (r)	0.29	0.14	0.08	0.16	7.90	1.72	0.77	0.03	2.16	0.72	2.35	1.21	0.50	0.36	0.57	1.34	0.62	0.68
	O VIII (K $\alpha$ )	0.34	0.07	0.03	0.05	0.74	0.25	0.38	0.01	2.81	0.38	5.22	1.76	0.22	0.17	0.90	2.12	1.38	0.96
	0.4–0.85 keV	8.10	2.34	1.51	2.47	14.25	5.73	8.65	0.39	11.85	7.50	16.84	9.05	1.93	0.30	2.47	4.54	2.43	2.33
	0.1–2 keV	2.61	1.57	0.86	1.38	4.48	2.18	1.27	0.15	1.91	1.55	2.75	1.53	1.40	0.47	1.36	3.04	1.80	1.61
Diffuse gas	O VII (r)	1.06	2.09	1.23	1.15	8.89	2.88	4.64	10.53	4.85	1.26	4.29	5.11	1.47	4.06	1.83	1.83	8.00	3.44
	O VIII (K $\alpha$ )	2.03	1.92	0.74	1.03	1.04	1.35	3.82	6.86	45.00	1.07	4.88	12.33	1.31	7.11	8.20	1.75	3.74	4.42
	0.4–0.85 keV	51.32	18.44	13.63	14.34	39.77	27.50	66.27	129.44	81.67	14.62	17.01	61.80	9.03	15.58	12.83	4.71	29.63	14.36
	0.1–2 keV	9.74	4.08	3.15	3.54	9.93	6.09	5.84	11.67	7.20	1.80	2.12	5.72	3.66	6.41	5.23	2.60	13.09	6.20
All lightcone emission	O VII (r)	2.11	3.38	1.73	2.57	21.66	6.29	8.62	21.27	11.23	2.25	18.31	12.33	3.27	7.12	4.56	5.44	16.08	7.29
	O VIII (K $\alpha$ )	3.04	3.18	1.68	2.54	3.28	2.74	6.84	21.22	55.45	3.74	15.23	20.50	2.51	17.54	12.71	5.15	6.54	8.89
	0.4–0.85 keV	80.98	56.98	34.96	40.38	85.23	59.71	101.10	186.11	162.47	28.89	52.35	106.18	16.86	28.52	28.08	13.68	41.83	25.80
	0.1–2 keV	20.58	15.10	16.06	12.88	33.73	19.67	11.44	26.69	19.60	7.93	11.47	15.43	9.67	17.26	15.46	11.72	23.87	15.60

## 4. Discussion and conclusions

In this work, we used the TNG100 simulation to study the soft X-ray emissions from different intervening hot-gas components in a typical wide-field lightcone and estimate their impacts on spectral and flux measurements toward X-ray-emitting galaxy-, group- and cluster-halos at lower redshifts. In particular, we split the intervening hot gas into three categories, that is, the hot gas that is gravitationally bound to either star-forming or quenched galaxies, and the diffuse gas which is more tenuously distributed permeating the cosmic web structures. The main conclusions of this paper are as follows.

1. The total mass fraction of the diffuse gas in the lightcone is almost one order of magnitude higher than that of the gravitationally bound gas (as shown in Table 1), broadly consistent with the result using the TNG300 simulation by Galárraga-Espinosa et al. (2021). This diffuse component produces strong oxygen and iron line emissions at different redshifts in the soft X-ray band (as presented in Figs. 5, 6, and 7).
2. Hot gas that is gravitationally bound to galaxy halos and that is diffusely distributed as the intergalactic medium residing in the cosmic web structures occupy different regions of the temperature-density-metallicity phase space. Diffuse gas can contribute nearly equally to the soft X-ray emission comparing to the hot gas in star-forming galaxies along the line of sight, while quenched galaxy halos contribute the least to the hot gas emission in the lightcone (as shown in Table 2, as well as in Fig. 8 and Fig. 9).
3. The soft X-ray spectra and fluxes of the intervening hot gas differ strongly case by case due to the large variance in the foreground and background hot gas distributions in line with a target source (see Table 2). The fluxes from all of the line-of-sight emitters as measured in the energy band of 0.4–0.85 keV can reach  $\sim 20\text{--}200\%$  of the target emission, lower for clusters and higher for galaxies. The fluxes measured in narrow bands around the O VII ( $r$ ) and O VIII ( $K\alpha$ ) are typically a few percent of the target emission, indicating that these line emissions (as measured within narrow bands) better present the hot gas emission of the target sources, compared to that measured in wider energy bands.

This study targets at a theoretical investigation on the soft X-ray emission from line-of-sight origins. We note that the conclusions of this study are drawn using the TNG100 simulation. The quantitative details strongly depend on the implementation of hot gas physics. In particular, the strong metal emissions of the diffuse gas in the cosmic web structures are results of galactic feedback processes, which can discharge metals into these large distances from galaxy centers. To better understand the impacts of feedbacks on the distribution and properties of the hot gas, we should further compare other numerical cosmological simulations (e.g., EAGLE and SIMBA which adopt different models. From the observation perspective, the pioneering X-ray telescopes under planning, like *HUBS*, and *Super DIOS*, will provide us with valuable knowledge about the hot gas of different cosmic origins as well as deep insights about the baryonic cycle in galactic ecosystems.

**Acknowledgements.** The authors sincerely thank Dr. Junjie Mao for detailed and useful comments. The authors acknowledge the Tsinghua Astrophysics High-Performance Computing platform at Tsinghua University for providing computational and data storage resources that have contributed to the research results reported within this paper.

## References

- Anderson, M. E. & Bregman, J. N. 2011, *ApJ*, 737, 22
- Artale, M. C., Haider, M., Montero-Dorta, A. D., et al. 2022, *MNRAS*, 510, 399
- Ayromlou, M., Nelson, D., Pillepich, A., et al. 2024, *A&A*, 690, A20
- Bogdán, Á., Kraft, R. P., Evans, D. A., Andrade-Santos, F., & Forman, W. R. 2017, *ApJ*, 848, 61
- Bogdán, Á., Vogelsberger, M., Kraft, R. P., et al. 2015, *ApJ*, 804, 72
- Bregman, J. N. 2007, *ARA&A*, 45, 221
- Cen, R. & Fang, T. 2006, *ApJ*, 650, 573
- Cen, R. & Ostriker, J. P. 1999, *ApJ*, 514, 1
- Cen, R. & Ostriker, J. P. 2006, *ApJ*, 650, 560
- Chadayammuri, U., Bogdán, Á., Oppenheimer, B. D., et al. 2022, *ApJ*, 936, L15
- Crain, R. A., McCarthy, I. G., Frenk, C. S., Theuns, T., & Schaye, J. 2010, *MNRAS*, 407, 1403
- Cui, W., Bregman, J. N., Bruijn, M. P., et al. 2020a, in *Society of Photo-Optical Instrumentation Engineers (SPIE) Conference Series*, Vol. 11444, *Space Telescopes and Instrumentation 2020: Ultraviolet to Gamma Ray*, ed. J.-W. A. den Herder, S. Nikzad, & K. Nakazawa, 114442S
- Cui, W., Chen, L. B., Gao, B., et al. 2020b, *Journal of Low Temperature Physics*, 199, 502
- Das, S., Mathur, S., Nicastro, F., & Krongold, Y. 2019, *ApJ*, 882, L23
- Davé, R., Anglés-Alcázar, D., Narayanan, D., et al. 2019, *MNRAS*, 486, 2827
- Davé, R., Cen, R., Ostriker, J. P., et al. 2001, *ApJ*, 552, 473
- Davé, R. & Oppenheimer, B. D. 2007, *MNRAS*, 374, 427
- Davé, R., Oppenheimer, B. D., Katz, N., Kollmeier, J. A., & Weinberg, D. H. 2010, *MNRAS*, 408, 2051
- Davis, M., Efstathiou, G., Frenk, C. S., & White, S. D. M. 1985, *ApJ*, 292, 371
- Dekel, A. & Birnboim, Y. 2006, *MNRAS*, 368, 2
- Dekel, A., Birnboim, Y., Engel, G., et al. 2009, *Nature*, 457, 451
- Dolag, K., Borgani, S., Murante, G., & Springel, V. 2009, *MNRAS*, 399, 497
- Earl, N., Tollerud, E., Jones, C., et al. 2022, *astropy/specutils*: V1.6.0, Zenodo
- Efstathiou, G. 2000, *MNRAS*, 317, 697
- Faucher-Giguère, C.-A. & Oh, S. P. 2023, *ARA&A*, 61, 131
- Fielding, D. B., Tonnesen, S., DeFelippis, D., et al. 2020, *ApJ*, 903, 32
- Foster, A. R., Ji, L., Smith, R. K., & Brickhouse, N. S. 2012, *ApJ*, 756, 128
- Fukugita, M., Hogan, C. J., & Peebles, P. J. E. 1998, *ApJ*, 503, 518
- Galárraga-Espinosa, D., Aghanim, N., Langer, M., & Tanimura, H. 2021, *A&A*, 649, A117
- Genel, S., Nelson, D., Pillepich, A., et al. 2018, *MNRAS*, 474, 3976
- Haider, M., Steinhauser, D., Vogelsberger, M., et al. 2016, *MNRAS*, 457, 3024
- Hopkins, P. F., Chan, T. K., Ji, S., et al. 2021, *MNRAS*, 501, 3640
- Kastra, J., Finoguenov, A., Nicastro, F., et al. 2013, *arXiv e-prints*, arXiv:1306.2324
- Kang, H., Ryu, D., Cen, R., & Song, D. 2005, *ApJ*, 620, 21
- Kereš, D., Katz, N., Weinberg, D. H., & Davé, R. 2005, *MNRAS*, 363, 2
- Kitzbichler, M. G. & White, S. D. M. 2007, *MNRAS*, 376, 2
- Lehle, K., Nelson, D., Pillepich, A., Truong, N., & Rohr, E. 2024, *A&A*, 687, A129
- Li, J.-T., Bregman, J. N., Wang, Q. D., Crain, R. A., & Anderson, M. E. 2018, *ApJ*, 855, L24
- Li, J.-T., Bregman, J. N., Wang, Q. D., et al. 2017, *ApJS*, 233, 20
- Liu, A., Bulbul, E., Ghirardini, V., et al. 2022, *A&A*, 661, A2
- Locatelli, N., Ponti, G., Zheng, X., et al. 2024, *A&A*, 681, A78
- Lu, S., Xu, D., Wang, Y., et al. 2021, *MNRAS*, 503, 726
- Marinacci, F., Vogelsberger, M., Pakmor, R., et al. 2018, *MNRAS*, 480, 5113
- Martizzi, D., Vogelsberger, M., Artale, M. C., et al. 2019, *MNRAS*, 486, 3766
- Merloni, A., Predehl, P., Becker, W., et al. 2012, *arXiv e-prints*, arXiv:1209.3114
- Naiman, J. P., Pillepich, A., Springel, V., et al. 2018, *MNRAS*, 477, 1206
- Nandra, K., Barret, D., Barcons, X., et al. 2013, *arXiv e-prints*, arXiv:1306.2307
- Nelson, D., Byrohl, C., Ogorzalek, A., et al. 2023, *MNRAS*, 522, 3665
- Nelson, D., Kauffmann, G., Pillepich, A., et al. 2018a, *MNRAS*, 477, 450
- Nelson, D., Pillepich, A., Ayromlou, M., et al. 2024, *A&A*, 686, A157
- Nelson, D., Pillepich, A., Springel, V., et al. 2018b, *MNRAS*, 475, 624
- Nelson, D., Springel, V., Pillepich, A., et al. 2019, *Computational Astrophysics and Cosmology*, 6, 2
- Nicastro, F., Kaastra, J., Krongold, Y., et al. 2018, *Nature*, 558, 406
- Nicastro, F., Mathur, S., & Elvis, M. 2008, *Science*, 319, 55
- Nicastro, F., Mathur, S., Elvis, M., et al. 2005, *Nature*, 433, 495
- Oppenheimer, B. D., Bogdán, Á., Crain, R. A., et al. 2020a, *ApJ*, 893, L24
- Oppenheimer, B. D., Davies, J. J., Crain, R. A., et al. 2020b, *MNRAS*, 491, 2939
- Parekh, V., Laganá, T. F., Thorat, K., et al. 2020, *MNRAS*, 491, 2605
- Péroux, C. & Howk, J. C. 2020, *ARA&A*, 58, 363
- Phillips, L. A., Ostriker, J. P., & Cen, R. 2001, *ApJ*, 554, L9
- Pillepich, A., Nelson, D., Hernquist, L., et al. 2018a, *MNRAS*, 475, 648
- Pillepich, A., Springel, V., Nelson, D., et al. 2018b, *MNRAS*, 473, 4077
- Planck Collaboration, Ade, P. A. R., Aghanim, N., et al. 2013, *A&A*, 550, A134
- Planck Collaboration, Ade, P. A. R., Aghanim, N., et al. 2016, *A&A*, 594, A13
- Ponti, G., Sanders, J. S., Locatelli, N., et al. 2023, *A&A*, 670, A99
- Predehl, P., Andritschke, R., Arefiev, V., et al. 2021, *A&A*, 647, A1

- Prunier, M., Hlavacek-Larrondo, J., Pillepich, A., Lehle, K., & Nelson, D. 2025, *MNRAS*, 536, 3200
- Putman, M. E., Peek, J. E. G., & Joung, M. R. 2012, *ARA&A*, 50, 491
- Robson, D. & Davé, R. 2020, *MNRAS*, 498, 3061
- Rohr, E., Pillepich, A., Nelson, D., Ayromlou, M., & Zinger, E. 2024, *A&A*, 686, A86
- Ryden, B. & Pogge, R. W. 2021, *Interstellar and Intergalactic Medium* (Cambridge University Press)
- Sanders, J. S., Dennerl, K., Russell, H. R., et al. 2020, *A&A*, 633, A42
- Sarkar, K. C., Nath, B. B., Sharma, P., & Shchekinov, Y. 2016, *ApJ*, 818, L24
- Schaye, J., Crain, R. A., Bower, R. G., et al. 2015, *MNRAS*, 446, 521
- Schellenberger, G., Bogdán, Á., ZuHone, J. A., et al. 2024, *ApJ*, 969, 85
- Shull, J. M., Smith, B. D., & Danforth, C. W. 2012, *ApJ*, 759, 23
- Smith, R. K., Brickhouse, N. S., Liedahl, D. A., & Raymond, J. C. 2001, *ApJ*, 556, L91
- Springel, V. 2010, *MNRAS*, 401, 791
- Springel, V. & Hernquist, L. 2003, *MNRAS*, 339, 289
- Springel, V., Pakmor, R., Pillepich, A., et al. 2018, *MNRAS*, 475, 676
- Springel, V., White, S. D. M., Tormen, G., & Kauffmann, G. 2001, *MNRAS*, 328, 726
- Torrey, P., Vogelsberger, M., Marinacci, F., et al. 2019, *MNRAS*, 484, 5587
- Truong, N., Pillepich, A., Nelson, D., et al. 2024, *A&A*, 686, A200
- Truong, N., Pillepich, A., Werner, N., et al. 2020, *MNRAS*, 494, 549
- Tumlinson, J., Peebles, M. S., & Werk, J. K. 2017, *ARA&A*, 55, 389
- van de Voort, F. & Schaye, J. 2013, *MNRAS*, 430, 2688
- Vogelsberger, M., Sijacki, D., Kereš, D., Springel, V., & Hernquist, L. 2012, *MNRAS*, 425, 3024
- Wang, Q. D., Li, J., Jiang, X., & Fang, T. 2016, *MNRAS*, 457, 1385
- Weinberger, R., Springel, V., Hernquist, L., et al. 2017, *MNRAS*, 465, 3291
- Wiersma, R. P. C., Schaye, J., Theuns, T., Dalla Vecchia, C., & Tornatore, L. 2009, *MNRAS*, 399, 574
- Wijers, N. A. & Schaye, J. 2022, *MNRAS*, 514, 5214
- XRISM Science Team. 2020, arXiv e-prints, arXiv:2003.04962
- Yamada, S., Ohashi, T., Ishisaki, Y., et al. 2018, *Journal of Low Temperature Physics*, 193, 1016
- Yoshikawa, K., Yamasaki, N. Y., Suto, Y., et al. 2003, *PASJ*, 55, 879
- Yuan, F. & Narayan, R. 2014, *ARA&A*, 52, 529
- Yuan, F., Yoon, D., Li, Y.-P., et al. 2018, *ApJ*, 857, 121
- Zhang, Y., Comparat, J., Ponti, G., et al. 2024, *A&A*, 690, A267
- Zhang, Y.-N., Li, C., Xu, D., & Cui, W. 2022, *Experimental Astronomy*, 53, 1053
- Zhuravleva, I., Churazov, E., Schekochihin, A. A., et al. 2014, *Nature*, 515, 85
- Zhuravleva, I., Churazov, E., Schekochihin, A. A., et al. 2019, *Nature Astronomy*, 3, 832
- ZuHone, J. A., Vikhlinin, A., Tremblay, G. R., et al. 2023, *SOXS: Simulated Observations of X-ray Sources*, *Astrophysics Source Code Library*, record ascl:2301.024